Unsteady Flow Mechanisms of the Stability Improvement for an Optimized Compressor

T. Zhou[1], Z. X. Liu[1,2], X. J. Li[1,2†], M. Zhao[1,2], Y. J. Zhao[3] and L. C. Xu[1]

[1] School of Mechanical Engineering, Tianjin University, 300350 Tianjin, China
[2] National Key Laboratory of Vehicle Power System, Tianjin University, 300350 Tianjin, China
[3] School of Mechanical Engineering, Tianjin University of Commerce, 300134 Tianjin, China

†*Corresponding Author: lixiaojian@tju.edu.cn*

ABSTRACT

Radial compressor is a crucial component of turbocharging systems in aviation engines. Enhancing flow stability of radial compressor contributes to performances improvement of engines. Ported shroud (P-S) casing-treatment can effectively broaden the compressors flow stability range. However, the unsteady mechanisms of the P-S are still unclear. In this study, a collaborative optimization of the P-S and the impeller-diffuser is firstly carried out. The results show that the optimized compressor exhibits higher efficiency and larger flow stability range than the original and the solid-casing compressors. Then, the unsteady mechanisms of the flow stability enhancement for the optimized compressor are analyzed by the dynamic-mode-decomposition (DMD) method. It is found that the decrease of the energy proportion of the inherent mode and the increase of the low-frequency multi-scale modes are correlated to the flow instability of the compressor. The increased recirculating flow rate of the optimized compressor has removed more tip leakage flow (TLF) and double leakage flow (DLF) in the impeller inducer shroud, and then reduces the interplay among the TLF, the DLF and the leading-edge (LE) shock wave. Therefore, the generation of low-frequency multi-scale modes is suppressed, while the inherent modes are intensified. Consequently, the flow stability of the compressor is enhanced. This study may offer a new approach to enhance compressor stability by adjusting the energy proportions of inherent modes and low-frequency multi-scale modes.

1. INTRODUCTION

Due to the compact structure and high compression ratio, radial compressors find extensive applications in compact aircraft engines (Zhang et al., 2014). To attain higher efficiency and output power of engines, radial compressors tend to enhance the compression ratio and rotational speed. Consequently, the tip Mach number of compressors is significantly increased, which intensifies the interplay between the leading-edge (LE) shock wave, tip leakage vortex (TLV) and boundary layer separation. In turn, the flow stability of the compressors sharply decreases, making it challenging for aircraft engines to adapt to complex flight environments. Therefore, expanding the flow stability range of high-pressure-ratio radial compressors becomes crucial to enhance engines performances.

In recent years, numerous active and passive control strategies have been employed to boost the flow stability of high-pressure-ratio radial compressors (Tiainen et al., 2017). As an effective passive control strategy, the ported shroud (P-S) casing-treatment has garnered significant attentions. A P-S is usually composed of a bleeding slot, an injecting slot, and an annular chamber. Based on a summary of existing studies, the mechanisms for enhancing flow stability with P-S can be outlined as follows.

The first factor is the amount of recirculating flow rate of P-S (Lu et al., 2021). The greater the recirculating flow of the P-S, the more stagnant fluid is removed of the impeller inducer, resulting in a raised flow stability of the compressor. However, a large amount of recirculating flow will obviously strengthen the pre-swirl effect of the impeller inlet, and reduce the Euler work of the

NOMENCLATURE			
b_1	impeller trailing-edge tip installation angle	m_{11}	injecting slot angle
b_2	impeller trailing-edge hub installation angle	SP	stability parameter
b_3	impeller LE backsweep angle	V_{mode}	energy reduction rate of the inherent mode
b_4	diffuser trailing-edge radiu	W_{sr}	stability range
b_5	diffuser blade installation angle	π	pressure ratio
B	blockage percentage	η	efficiency
m	mass flow rate	BPF	Blade Passing Frequency
m_1	radial position of the annular chamber,	DMD	Dynamic-Mode-Decomposition
m_2	injecting slot radius	DLF	Double Leakage Flow
m_3	annular chamber height,	LE	Leading-Edge
m_4	annular chamber length	NS	Near Stall
m_5	bleeding slot angle	P-S	Ported Shroud
m_6	bleeding slot width	PE	Peak Efficiency
m_7	bleeding slot position	RANS	Reynolds-Averaged Navier-Stokes
m_8	injecting slot position	S-A	Spalart-Allmaras
m_9	bypass angle I	TLF	Tip Leakage Flow
m_{10}	bypass angle II	TLV	Tip Leakage Vortex

compressor (Yang et al., 2003; Wang et al., 2018; Khaleghi, 2020; Yan & Chu 2021). Also, the mixing of the recirculating flow and the impeller inlet flow will lead to greater aerodynamic loss.

The second factor of improving compressor stability by P-S is the improvement of the relative Mach number and shock wave near the impeller LE. The pre-swirl effect of recirculating fluid can reduce the impeller inlet relative Mach number and shock wave. Therefore, the TLV breakdown and boundary layer separation caused by the shock wave are suppressed, and the flow stability of the compressor is enhanced (Peng et al., 2021; Ding et al., 2022; Li et al., 2022a). However, this does not mean that smaller shock wave leads to better flow stability. For example, Tamaki (2012) found that installing guide vanes in the annular chamber of P-S has created a negative pre-swirl at the impeller inlet. It will increase the tip Mach number near the impeller LE, but it can finally boost the flow stability. The possible reason is that although shock wave is enhanced, its spatial distribution is more reasonable. The third factor is the impact of P-S on the radial distortion and circumferential non-uniformity of the impeller inlet flow. The interplay between the negative pre-swirl flow and the main flow damages the radial uniformity at the impeller inlet. Li et al. (2022b) demonstrated that reducing the bleeding slot angle of P-S can weaken the radial distortion at the impeller inlet and enhance the compressor flow stability.

Nevertheless, the above mechanisms for boosting flow stability of radial compressors are based on a steady perspective. In fact, the flow instabilities in radial compressors exhibit significant unsteady characteristics, including LE flow spillage, trailing-edge backflow, TLV breakdown, LE flow separation, and tornado vortex formation, etc. (Vo et al., 2008; Hazy & Xu, 2009; Yamada et al., 2012, 2013). Therefore, it is necessary to explore the unsteady flow mechanisms of compressor stability enhancement. This aids the development of more robust methods to improve compressor flow stability while minimizing impacts on aerodynamic performances. However, the researches on this aspect are rare.

This study carries out a collaborative optimization of P-S and the impeller-diffuser for a transonic radial compressor, to achieve the goal of expanding the stall margin while keeping the efficiency within the full working range. Then, the unsteady mechanisms of the flow stability enhancement are analyzed by the dynamic-mode-decomposition (DMD) method.

2. NUMERICAL METHOD AND VALIDATION

As shown in Fig. 1, the original compressor is composed of three parts: impeller, vaned diffuser and P-S. Table 1 displays the design parameters of the original compressor.

The geometric model and experimental data of the original compressor come from China North Engine Research Institute. Pressure sensors and thermocouples are used to accurately measure the total pressure ratio and temperature at the impeller inlet and the vaned diffuser outlet. The mass flow rate is measured by a mass flow meter, and the outlet pressure is controlled by an adjustable back-pressure valve to obtain comprehensive pressure ratio curves. The experiments are conducted across multiple operating conditions, with rotational
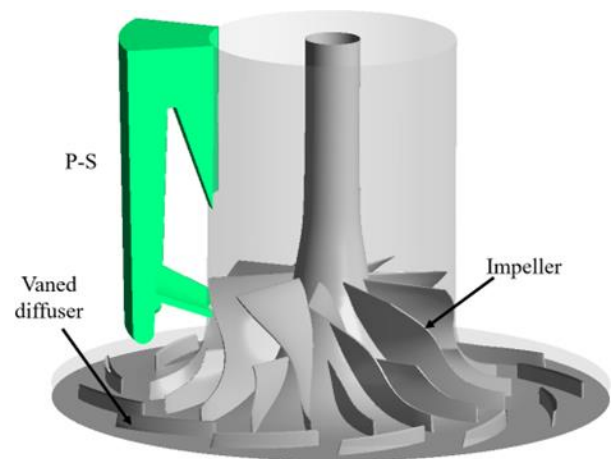

Fig. 1 Solid model of the original compressor

Table 1 Main design parameters of the original compressor

Parameters	Values
Rated speed	94500 rpm
Tip Mach number	1.7
Flow rate of peak efficiency point	0.881 kg/s
Impeller exit diameter	118 mm
Diffuser trailing-edge diameter	200 mm
Number of full/splitter blades	9/9
Number of diffuser vanes	12
Tip clearance	0.5 mm

speeds ranging from 60% to 110% of the design speed. Experimental data is collected and processed in real-time to generate performance curves, ensuring accurate and reliable analysis of compressor performances.

The commercial software suit ANSYS CFX is used for the grid generation and numerical calculations. Considering the periodic characteristic of the compressor, single-passage numerical model has been used for calculation to conserve computational resources. The Spalart-Allmaras (S-A) turbulence model is adopted to solve the Reynolds-averaged Navier-Stokes (RANS) equations. Spatial discretization adopts the second-order upwind-central difference scheme, while temporal discretization employs the implicit second-order backward Euler method. In numerical calculations, the inlet total pressure and temperature of the compressor are 101325 Pa and 298.15 K. The boundary conditions at the diffuser outlet are specified as either static pressure or mass flow rate depending on the operating conditions of the compressor.

The non-slip and adiabatic condition is employed for solid walls. The frozen rotor interface type is employed for the impeller and the P-S, as well as the vaned diffuser and the volute. For steady-state calculations, the mixing plane method is adopted for the impeller and the vaned diffuser. For unsteady calculations, the interface type between the impeller and the vaned diffuser is the transient-rotor-stator. The physical time step is set as 1.76×10^{-6} s in the unsteady simulations.

Three different meshes with 1.24 million, 2.06 million and 3.15 million cells respectively are selected for mesh independence verification of the compressor. The three grids possess the same first layer thickness (5.5×10^{-6} m), corresponding to the y plus less than 3. Figure 2 illustrates that the mesh with 2.06 million cells is sufficient to ensure the calculation accuracy. Therefore, this mesh is chosen for further calculations. Figure 3 displays the medium grid of the compressor.

Figure 4 illustrates the comparisons of pressure ratio (π) curves at different speeds between the simulated and experimental data. The simulated data generally aligns with the experimental data. Particularly, at the rated speed (94500 rpm) the maximum relative error between the simulated and experiment data is only 1.89%. Hence, the simulation approach employed in this study is sufficiently

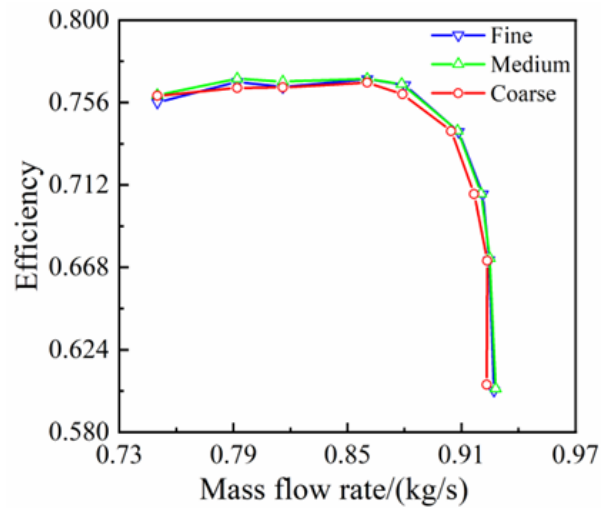accurate and can provide reliable performances predictions for the compressor.

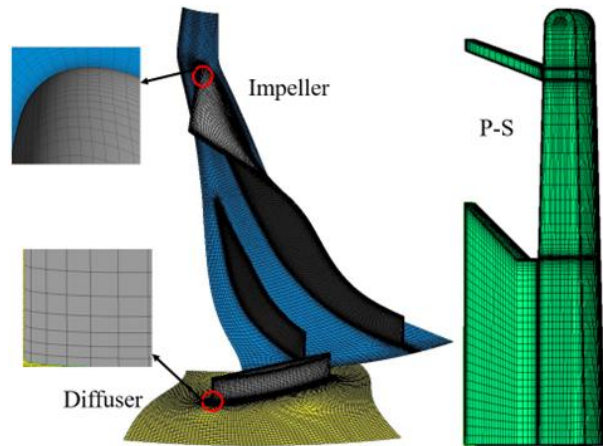**Fig. 2 Grid independence verification**

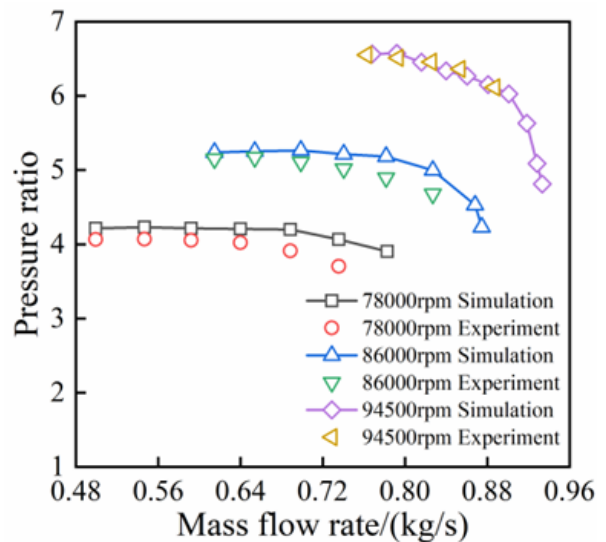**Fig. 3 The grid topology of the compressor**

Fig. 4 Comparisons of pressure ratio curves between simulation and experiment at different rotating speeds
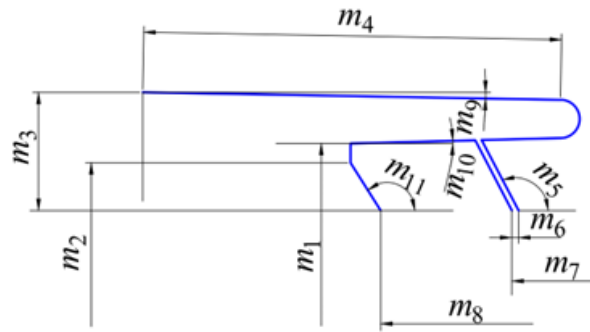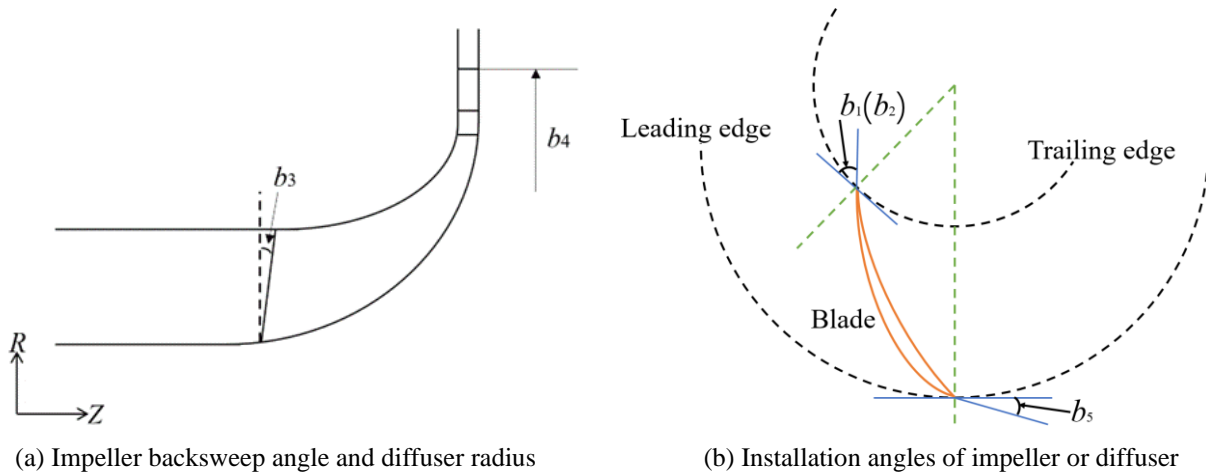
Fig. 5 Optimization variables of the P-S

(a) Impeller backsweep angle and diffuser radius

(b) Installation angles of impeller or diffuser

Fig. 6 Optimization variables of the impeller-diffuser

3. MULTI-COMPONENT COLLABORATIVE OPTIMIZATION OF COMPRESSOR

In this part, a collaborative optimization is carried out at the rated speed (94500rpm), and the optimization results are analyzed.

3.1 Optimization Setup and Implementation

The components involved in the collaborative optimization of the compressor include impeller-diffuser and P-S. Initially, the design space for collaborative optimization is established. Figure 5 shows the 11 parameters of the P-S. They are the radial position of the annular chamber (m_1), the injecting slot radius (m_2), the annular chamber height (m_3), the annular chamber length (m_4), the bleeding slot angle (m_5), the bleeding slot width (m_6), the bleeding slot position (m_7), the injecting slot position (m_8), the bypass angle I (m_9), the bypass angle II (m_{10}) and the injecting slot angle (m_{11}).

As for the impeller-diffuser, according to the references (Hazy & Xu, 2009; Boccazzi et al., 2011; He & Zheng 2017; Li et al., 2017, 2019), the impeller trailing-edge tip and hub installation angles (b_1, b_2), the impeller LE backsweep angle (b_3), the diffuser trailing-edge radius (b_4) and the diffuser blade installation angle (b_5) are potential key variables that impact compressor performances. Figure 6 displays the diagrams of these optimization variables of the impeller-diffuser. The efficiency (η) and pressure ratio (π) at the peak efficiency (PE) point (0.881kg/s) and the near stall (NS) point (0.792 kg/s) as well as the choke flow rate (m_{choke}) are selected as the indexes to reflect the compressor performances. Therefore, 16 optimization variables (m_1, m_2, … m_{11}, b_1, b_2, … b_5) and 5 performance indexes (η_{PE}, π_{PE}, η_{NS}, π_{NS}, m_{choke}) of the compressor constitute the design space of the collaborative optimization.

To simplify the design space for collaborative optimization, global sensitivity analysis is employed to quantitatively identify the key optimization variables. The analysis of variance (ANOVA) method is selected for sensitivity analysis. The detailed theory of ANOVA can be found in reference (Cios et al., 2007). The variables ranges for the global sensitivity analysis are determined according to the compressor geometry constraints. Table 2 displays the value interval and the original value of the 16 optimization variables.

Figure 7 shows the effects of the optimization variables on the five performance indexes. It is found that three optimization variables of the P-S (m_6, m_7, m_{11}) and four of the impeller-diffuser (b_1, b_2, b_3, b_4) have greater impacts on the compressor performances (>10%), and they are considered as key variables of performance indexes (Zhao et al., 2023). Therefore, the seven key optimization variables (m_6, m_7, m_{11}, b_1, b_2, b_3, b_4) are ultimately determined for the collaborative optimization.

Table 2 The value interval and the original value for the 16 optimization variables of the compressor

Optimization variables	Lower limits	Original values	Upper limits
m_1 /mm	57.70	58.11	64.00
m_2 /mm	46.00	52.76	60.00
m_3 /mm	26.50	29.55	36.00
m_4 /mm	86.40	95.00	102.50
m_5 /deg	92.00	111.60	132.00
m_6 /mm	1.10	2.60	3.85
m_7 /mm	-34.00	-31.15	-26.00
m_8 /mm	-75.00	-65.55	-56.00
m_9 /deg	0.50	1.54	3.00
m_{10} /deg	0.05	1.59	2.90
m_{11} /deg	123.00	138.00	160.00
b_1 /deg	43.00	44.80	46.00
b_2 /deg	53.70	55.20	56.20
b_3 /deg	1.00	5.00	5.00
b_4 /mm	78.66	79.00	81.76
b_5 /deg	64.30	66.20	68.20

(a) $m_{choke}^{\&}$ (b) η_{PE} (c) η_{NS}
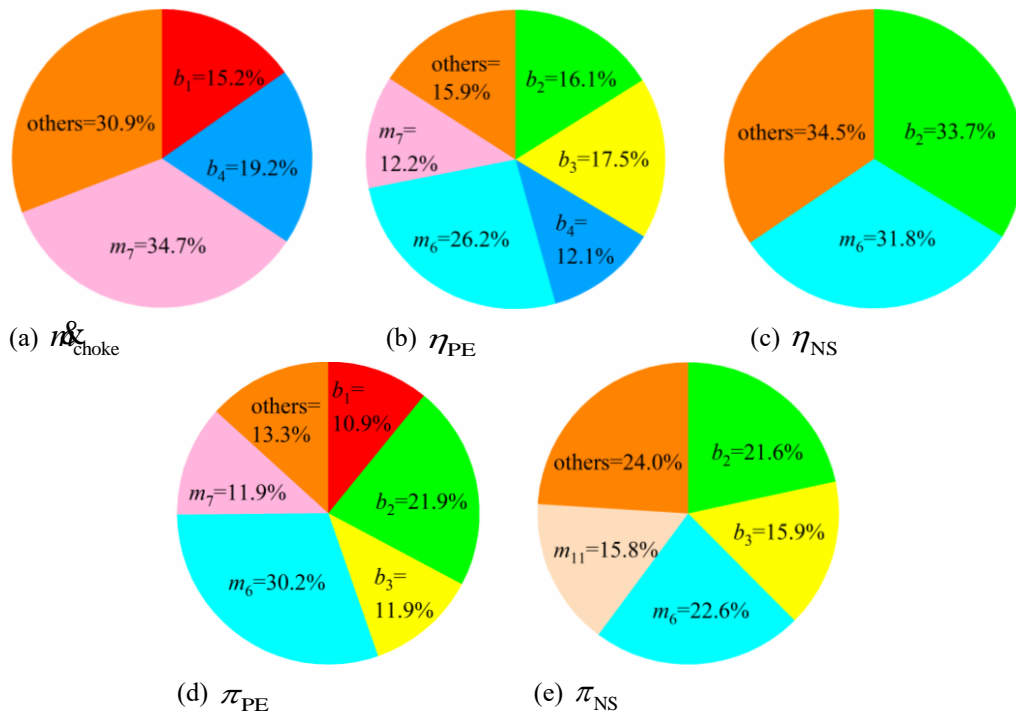
(d) π_{PE} (e) π_{NS}

Fig. 7 Influence degree of optimization variables on compressor performance indexes

The collaborative optimization of the compressor can be abstracted as follows

Maximization：

$$\begin{cases} \eta_{PE} = f_1(m_6, m_7, m_{11}, b_1, b_2, b_3, b_4) \\ \eta_{NS} = f_2(m_6, m_7, m_{11}, b_1, b_2, b_3, b_4) \end{cases}$$

Constraints：

$$\begin{cases} \pi_{PE} > \pi_{PE, \, original} \\ \pi_{NS} > \pi_{NS, \, original} \\ \pi_{NS} > \pi_{PE} \\ m_{choke} > m_{choke, \, original} \end{cases} \tag{1}$$

The efficiencies at the PE point (0.881kg/s) and NS point (0.792kg/s) are maximized. The constraints are that the pressure ratio π must exceed the original values at both the PE and the NS points, the π at the NS point is higher than that at the PE point, and the choke flow rate should exceed the original value. An in-house hybrid optimization algorithm is used to solve the collaborative optimization problem. The hybrid algorithm incorporates a gradient mutation operator into the traditional NSGA-II multi-objective genetic algorithm. The gradient mutation operator implements directional mutations with a specified step size based on the gradient descent direction, which notably enhances the convergence speed. Simultaneously, the inclusion of random crossover and random mutation helps the algorithm avoid getting
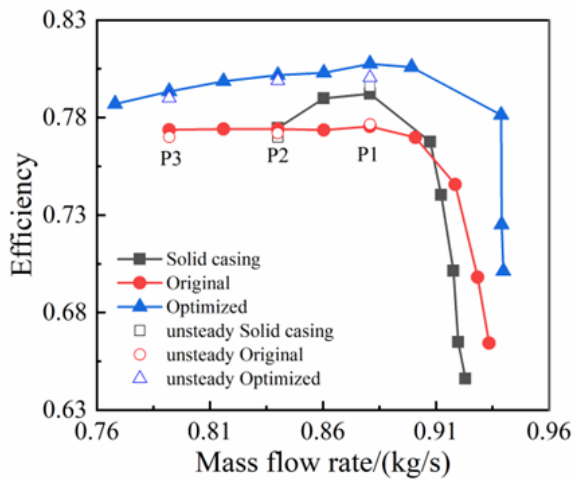
(a) Efficiency
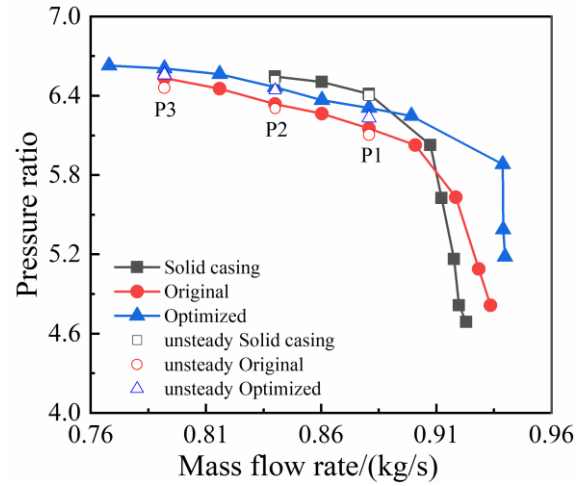
(b) Pressure ratio

Fig. 8 Comparisons of characteristic curves among the three compressors at the rated speed

Table 3 Comparisons of the η and W_{sr} among the three compressors

	Solid casing	Original	Optimized	Improvement of Solid casing versus Original	Improvement of Optimized versus Solid casing	Improvement of Optimized versus Original
η_{P1}	79.22%	77.54%	80.76%	-1.68%	1.54%	3.22%
η_{P2}	77.47%	77.42%	80.18%	-0.05%	2.71%	2.76%
η_{P3}		77.37%	79.35%			1.98%
W_{sr}	8.99%	15.16%	18.28%	6.17%	9.29%	3.12%

trapped in local optimums. As a result, this hybrid optimization approach has the potential to significantly boost search efficiency while preserving robust global performance. Previous studies (Tamaki, 2012; Zhou et al., 2021; Li et al. 2022b; Zhao et al., 2023) have shown that the hybrid algorithm can ensure the diversity of the optimal solution set while improving the optimization speed.

3.2 Optimization Results

Figure 8 presents the characteristic curves of the original and the optimized compressors, and the one with solid casing (just removing the P-S from the original compressor). Figure 8(a) indicates that the optimized compressor exhibits higher efficiency than the original compressor and the solid casing compressor over the entire operating range. Figure 8(b) illustrates that the pressure ratio of the optimized compressor exceeds the original compressor across the full operating range, and its peak value surpasses the solid casing compressor.

Three typical operating conditions (P_1=0.881 kg/s, P_2=0.840 kg/s, P_3=0.792 kg/s) are selected to analyze the performances of the three compressors, where P_1, P_2 and P_3 represent the PE point, the small flow rate (SFR) point, and the NS point of the original compressor respectively. The stability range of the compressor is assessed by (Favaretto et al., 2018; Zhao et al., 2023)

$$W_{sr} = \frac{m_{choke} - m_{NS}}{m_{choke}} \qquad (2)$$

where m_{choke} is the choke flow rate and m_{NS} is the NS flow rate.

Table 3 compares the efficiency at P_1, P_2, P_3 conditions (η_{P1}, η_{P2}, η_{P3}) and the stability range (W_{sr}) among the three compressors. In comparison to the original compressor, the efficiency of the optimized compressor is increased by 3.22%, 2.76%, and 1.98% under the three conditions, and the W_{sr} is improved by 3.12%. When compared to the solid casing compressor, the optimized compressor has improved the efficiency by 1.54% and 2.71% at P_1 and P_2 conditions respectively, while the original compressor introduces some aerodynamic losses in the corresponding conditions (decreased by 1.68% and 0.05% respectively). Fig. 8 and Table 3 demonstrate that the collaborative optimization has achieved the dual goal of flow stability expansion and aerodynamic performance improvements.

As stated in Introduction, this study aims to reveal the unsteady mechanisms behind the enhancement of flow stability after collaborative optimization. Therefore, it is essential to verify that the flow stability of the optimized compressor is genuinely enhanced. Although the W_{sr} indicates an improvement in flow stability, it is a global criterion and does not reflect the specific flow characteristics. The flow field improvements should be analyzed to demonstrate the flow stability enhancement. Note that the analyses in the following context of this subsection (Section 3.2) are all based on the steady simulation results.
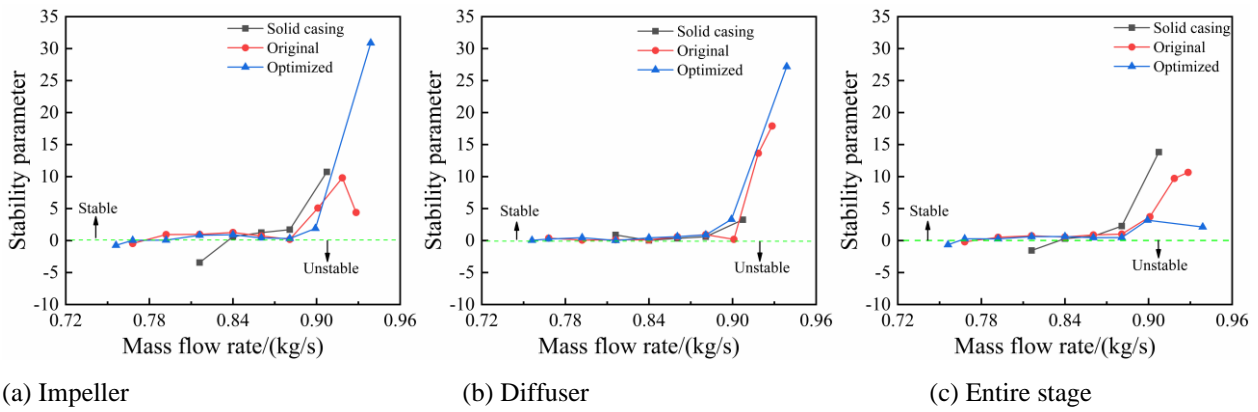
(a) Impeller	(b) Diffuser	(c) Entire stage

Fig. 9 The *SP* of components for the compressor

Table 4 Blockage percentage at 95% span of the compressors under P$_2$ and P$_3$ conditions

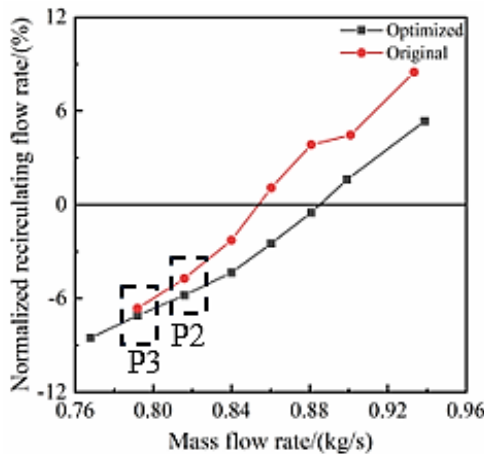|	Solid casing	Original	Optimized	Improvement of Solid casing versus Original	Improvement of Optimized versus Solid casing	Improvement of Optimized versus Original
B_{P2}	19.90%	18.95%	15.38%	4.79%	22.73%	18.84%
B_{P3}		21.97%	17.18%			21.83%

Fig. 10 Comparisons of the recirculating flow rates of the P-S between the original and the optimized compressors

However, the flow stability improvement might be related to the impeller or the vaned diffuser. To identify the component responsible for the stability improvement, the stability parameters *SP* (Shu et al., 2018; Xu et al., 2023b) is calculated for the impeller, the vaned diffuser and the entire stage. *SP* is defined as Shu et al. (2018)

$$SP = -\sum_{i}^{n} \frac{1}{\pi_i} \frac{\partial \pi_i}{\partial \dot{m}} \qquad (3)$$

where π is the pressure ratio and $\dot{m}$ is the mass flow rate of the component, and *i* represents a certain part of the compressor or the entire stage. If the *SP* is positive, the component is stable; otherwise, it is unstable.

Figure 9 displays the *SP* of the impeller, diffuser, and the entire stage. The *SP* of the impeller is generally

consistent with that of the entire stage for the three compressors. This means that the impeller dominants the flow stability of the entire stage. Therefore, the flow fields of the impeller will be analyzed in detail.

According to the reference (Huang et al., 2020), the improvement in compressor flow stability is usually characterized by a higher recirculating flow rate of P-S and a reduced passage blockage in the impeller. Figure 10 displays the variation of the recirculating flow of the P-S. It is normalized by the corresponding mass flow rate of the compressor (Li et al., 2022b). The negative recirculating flow rates denote suction effect of the P-S. As illustrated in Fig. 10, the P-S of the optimized compressor exhibits higher recirculating flow rate than the original compressor in small flow rate points (≤0.84kg/s). Hence, the optimized compressor possesses larger stall margin.

To evaluate the passage blockage of impeller inducer, a blockage percentage (Yan & Chu, 2021) is defined as

$$B = \frac{S_B}{S_{passage}} \times 100\% \qquad (4)$$

where, S_B is the area of the region with negative streamwise velocity, and $S_{passage}$ is the total area of the impeller passage. Table 4 displays the blockage percentage at 95% span of the compressors under P$_2$ and P$_3$ conditions. It is found that the blockage percentages of the optimized compressor at P$_2$ and P$_3$ conditions are decreased by 18.84% and 21.83% respectively compared to the original compressor. This is due to the enhanced suction effect of the P-S of the optimized compressor (see Fig. 10), allowing more stagnant fluid in impeller inducer to be removed. To further confirm this, Fig. 11 depicts the streamwise velocity at 95% span of the impeller under the P$_2$ and P$_3$ conditions. The blue region is the area with
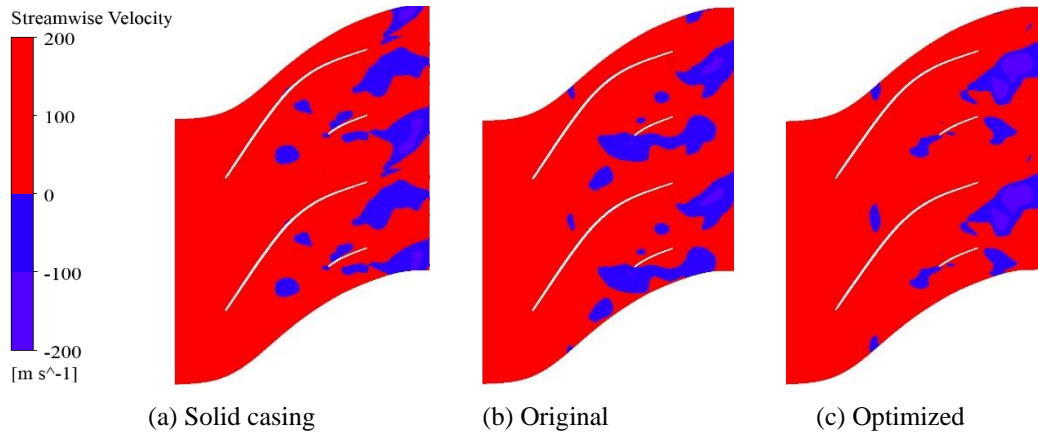
(a) Solid casing   (b) Original   (c) Optimized

Fig. 11 Streamwise velocity at 95% span of the impeller at P₂

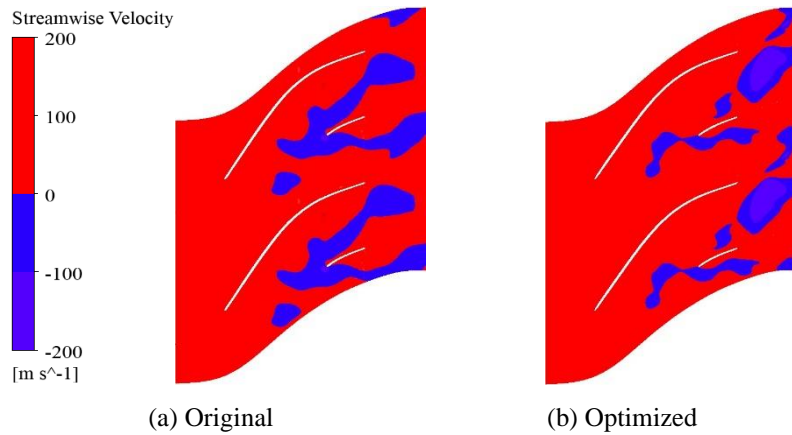(a) Original   (b) Optimized

Fig. 12 Streamwise velocity at 95% span of the impeller at P₃

negative streamwise velocity, which is highly correlated to the passage blockage. The results show that the negative streamwise velocity region of the optimized compressor is reduced. This also holds true for Fig. 12.

The above analyses prove that the collaborative optimization has significantly improved the flow stability of the compressor. The analyses regarding the unsteady mechanisms of stability enhancement for the optimized compressor will be presented in the next section.

4. UNSTEADY MECHANISMS OF STABILITY ENHANCEMENT

In this section, the dynamic-mode-decomposition (DMD) method is employed to elucidate the unsteady mechanisms of stability enhancement for the optimized compressor from the perspective of dominant modes.

4.1 DMD Method

The DMD method based on Singular Value Decomposition (SVD) is employed for unsteady mechanisms analyses. A detailed introduction to this method can be found in reference (Schmid, 2010).

The sample of the unsteady flow field obtained by numerical simulation or experimental method can be expressed as $x_1, x_2, ..., x_n$, where $x_i \in £^z$ is the ith

flow field sample, z is the number of spatial points in a flow field sample, n is the number of flow field samples, and the time step between each sample is Δt. It assumes that two adjacent samples satisfy linear relationship as follow

$$x_{i+1} = A x_i \tag{5}$$

The matrix $A \in £^{z \times z}$ contains the dynamic characteristics of the flow field (Huang et al. 2020). If considering the flow field sample sequence

$$
\begin{aligned}
X &= \left[x_1, \, x_2, \, ..., \, x_{n-1} \right] \\
X' &= \left[x_2, \, x_3, \, ..., \, x_n \right]
\end{aligned}
\tag{6}
$$

where the matrices X and X' are exactly staggered by one time step, then the relation between X and X' can be expressed as

$$X' = AX \tag{7}$$

To obtain the dynamic characteristics of matrix A, its similarity matrix A' can be obtained from Eq. (8) by a similarity transformation

$$A = U A' U^H \tag{8}$$

Implementing SVD operation on matrix X, it yields

$$X = U \Sigma V^H \tag{9}$$

where U and V are unitary matrices obtained by SVD operation (Taira et al., 2017), which satisfy the $U^H U = I$ and $V^H V = I$ (I is a unit matrix) (Taira et al., 2017), Σ is a diagonal matrix consisting of r singular values (Sesterhenn & Shahirpour, 2019).

According to Eq. (7), the matrix A can be written as

$$A = X' X^{-1} \tag{10}$$

Substituting Eq. (9) into (10) yields

$$A = X' V \Sigma^{-1} U^H \tag{11}$$

The matrix A' is obtained by projecting matrix A onto matrix U (Xu et al. 2023a)

$$A' = U^H A U = U^H X' V \Sigma^{-1} \tag{12}$$

The eigenvalues and eigenvectors of A' are written as

$$A' W = W \Lambda, \quad \Lambda = \text{diag}(\lambda_1, \lambda_2, L, \lambda_r) \tag{13}$$

Combining Eqs. (11), (12) and (13), it yields

$$A X' V \Sigma^{-1} W = X' V \Sigma^{-1} W \Lambda \tag{14}$$

Then, the DMD modes can be represented by

$$\Phi = X' V \Sigma^{-1} W \tag{15}$$

The mode frequency can be obtained by

$$\mu_i = \ln(\lambda_i) / \Delta t = \mu_i^r + \mu_i^i \tag{16}$$

where λ_i is the eigenvalue of Λ, μ_i^r and μ_i^i represent the growth rate and characteristic frequency of the modes respectively (Lyu et al., 2022).

The amplitude vector α of the modes is defined as

$$\Phi \alpha = x_1 \tag{17}$$

where α can be calculated by the least-squares method (Wu et al., 2021) as follow

$$\alpha = \Phi^{-1} x_1 \tag{18}$$

Therefore, x_i can be derived as

$$x_i = \Phi \Lambda^{i-1} \alpha = \sum_{j=1}^{r} \Phi_j \left(\lambda_j \right)^{i-1} \alpha_j \tag{19}$$

Then matrix X is reconstructed as

$$X = \left[x_1, x_2, ..., x_{n-1} \right] = \Phi D_\alpha V_{\text{and}} \tag{20}$$

where $D_\alpha = \begin{pmatrix} \alpha_1 & & \\ & O & \\ & & \alpha_r \end{pmatrix}$, $V_{\text{and}} = \begin{pmatrix} 1 & \lambda_1 & L & \lambda_1^{n-2} \\ M & M & & M \\ 1 & \lambda_r & L & \lambda_r^{n-2} \end{pmatrix}$

By following Kou & Zhang (2017) and Xu et al (2023a), the energy of the jth mode is written as

$$Q_j = \sum_{i=1}^{N} \left| \alpha_j \left(\mu_j \right)^{i-1} \right| \left\| \Phi_j \right\|_F^2 \Delta t \tag{21}$$

The importance of the jth mode is assessed by the mode energy proportion E_j as follows

$$E_j = \frac{Q_j}{\sum_{j=1}^{r} Q_j} \tag{22}$$

4.2 Unsteady Mechanisms of Stability Enhancement

As suggested in Section 3.2, the enhancement of compressor flow stability is closely related to the flow field improvement in impeller tip regions. Therefore, the unsteady flow analyses mainly focus on these regions. 450 flow field samples (5 rotations of the compressor) of the relative velocity at 95% span of the impeller are collected for the DMD analyses. The time-interval between each sample is $\Delta t = 4 \Delta t_s$, where Δt_s is the physical time step of unsteady numerical simulation of the compressor.

Figure 13 illustrates the energy proportions of the three compressors impeller at 95% span under different working conditions, in which the region within the dashed box is enlarged. It can be found that the energy proportions of BPF (blade passing frequency) and nBPF modes are dominant among the three compressors. BPF/nBPF modes structures are generated due to the interplays between impeller and diffuser (Trébinjac et al., 2009; Zamiri et al., 2017). They are inherent modes and do not influence the flow stability of the compressor (Li et al., 2021).

With the decrease of mass flow rate (from P_1 point to P_3 point), the energy proportions of the inherent modes decline, whereas these of the low-frequency modes rise. The energies of the inherent modes appear to transfer towards the low-frequency modes. At the same time, the stability of the compressor decreases. The greater the energy transfer is, the worse the flow stability of the compressor will be. Therefore, the deterioration in flow stability has a strong correlation with the energy transfer from the inherent modes to the low-frequency modes.

To quantitatively estimate the energy transfer, an energy reduction rate of the inherent mode (V_{mode}) is defined as follow

$$V_{\text{mode}} = \frac{E_{\text{BPF, P1}} - E_{\text{BPF, P2}}}{E_{\text{BPF, P1}}} \times 100\% \tag{23}$$

where $E_{\text{BPF, P1}}$, $E_{\text{BPF, P2}}$ are the energy proportions of the BPF mode in P_1 and P_2 working conditions respectively.

Table 5 compares the energy proportions of the BPF under the P_1 and P_2 conditions ($E_{\text{BPF, P1}}$, $E_{\text{BPF, P2}}$) and the corresponding energy reduction rates (V_{mode}). It is clear that the optimized compressor possesses the largest energy proportion of inherent modes and the smallest

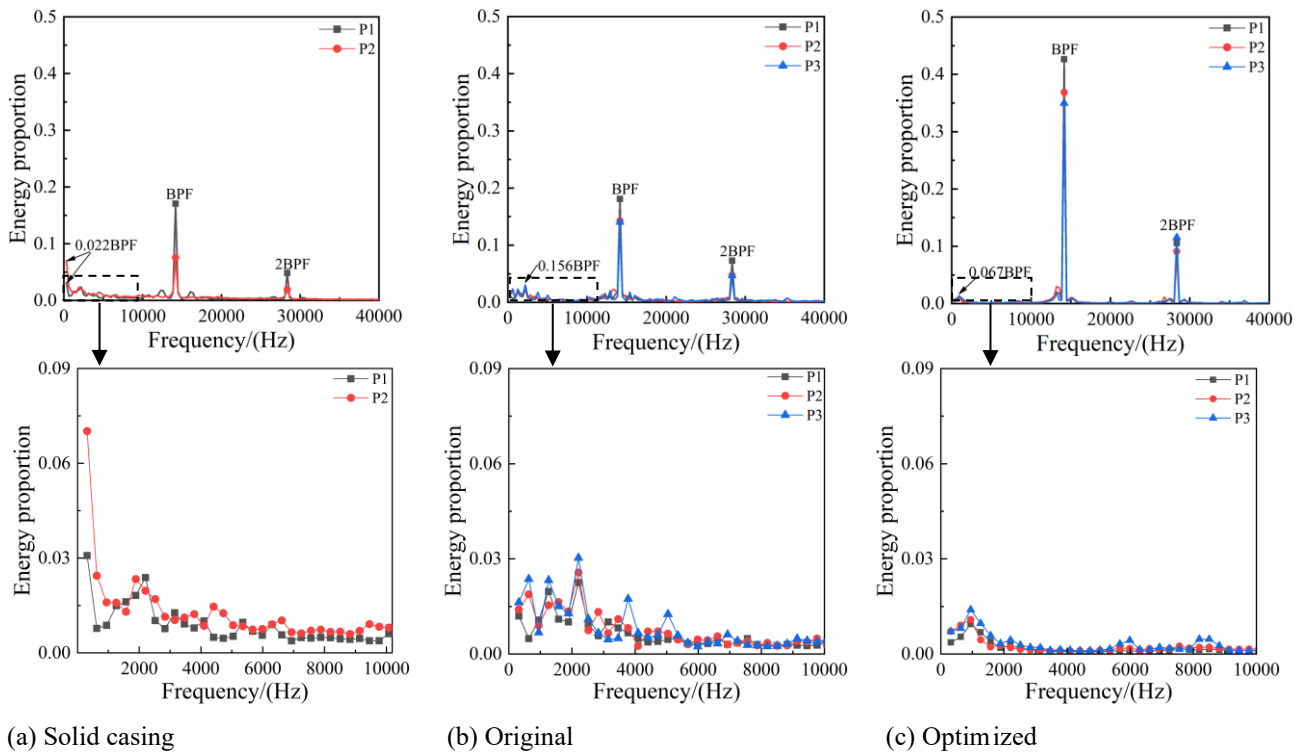(a) Solid casing   (b) Original   (c) Optimized

Fig. 13 Energy proportions of the three compressors impeller at 95% span under different working conditions
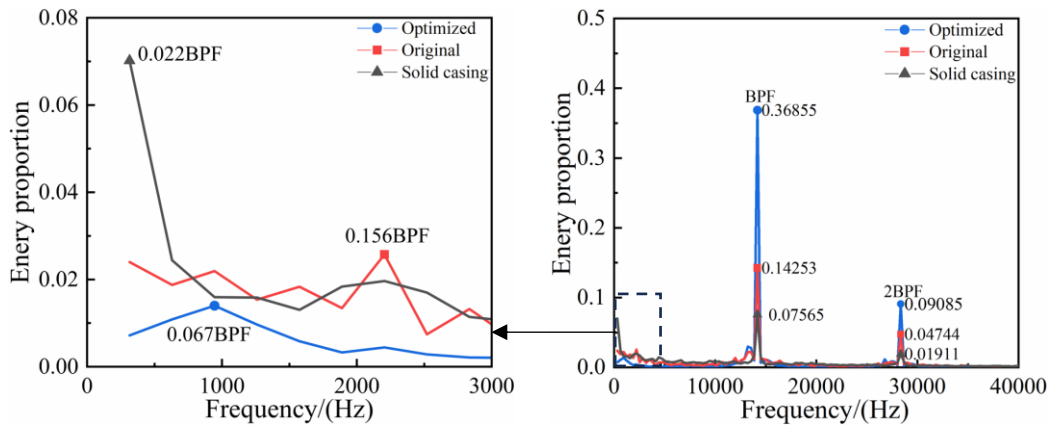

Fig. 14 Energy proportions of the three compressors impeller at 95% span under the P_2 working condition

Table 5 Energy reduction ratio of the inherent modes and BPF energy proportion of the three compressors

	$E_{BPF, P1}$	$E_{BPF, P2}$	V_{mode} (%)
Solid casing	0.171	0.076	55.56
Original	0.181	0.143	20.99
Optimized	0.426	0.369	13.38

energy reduction rate. However, this is totally opposite for the solid casing compressor. This indicates that the optimized compressor can effectively suppress the transfer process of the mode energy. Therefore, the unsteady mechanism of flow stability enhancement for the

optimized compressor is that the energy transfer process of the inherent modes is suppressed.

Figure 14 compares the energy proportions among the three compressors impeller under the P_2 working condition, in which the low-frequency region is enlarged. The peak amplitudes of the low-frequency region for the solid casing, the original and the optimized compressors are 0.022BPF, 0.156BPF and 0.067BPF respectively, and they are considered as the low-frequency dominant (LFD) modes. As indicated in the figure, the energy proportion of low-frequency multi-scale modes in the optimized compressor is the lowest, while that of the solid casing compressor is the highest. This confirms that the optimized compressor can better suppress the growth of low-frequency multi-scale modes, especially for the LFD modes.
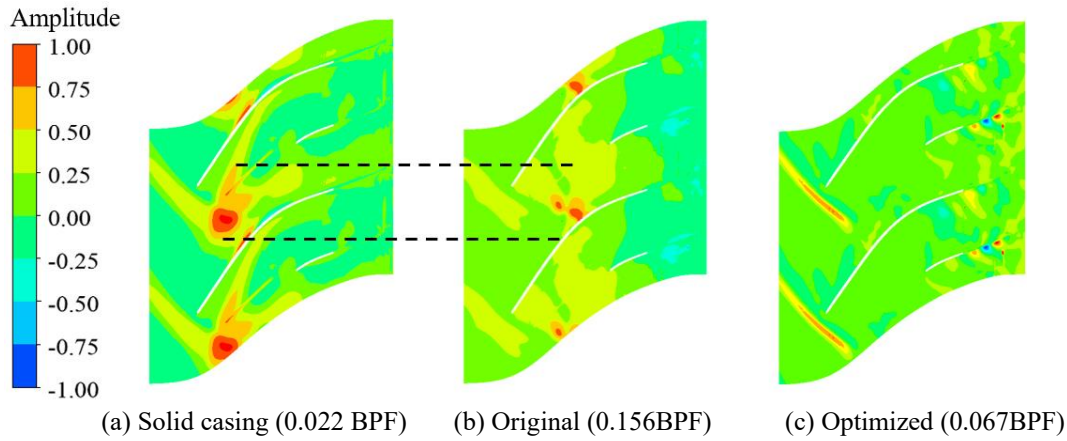
(a) Solid casing (0.022 BPF)   (b) Original (0.156BPF)   (c) Optimized (0.067BPF)

Fig. 15 Spatial structure of the LFD modes for the three compressors impeller at 95% span under the P$_2$ working condition

As suggested in the reference (Lin & Cheng, 2018), the interplays among tip leakage flow (TLF), LE shock wave, and double leakage flow (DLF) often exist at high span of impeller inducer, which leads to the appearance of strong unstable signals near the shroud. Recalling the above DMD analyses in impeller tip regions, it is inferred that the low-frequency modes with peak amplitudes (see Fig. 14) are likely to be related to these flow structures. Hence, the spatial structures of low-frequency modes are analyzed, and the interplays between mode structures and flow structures are discussed.

Figure 15 illustrates the spatial structure of peak amplitudes modes in low-frequency region for the three compressors. Figure 15(a) represents the structure of the 0.022BPF mode in the solid casing compressor. It is positioned at the passage center near the blade LE, obstructing a portion of the impeller inducer. Figure 15(b) depicts the structure of 0.156BPF mode in the original compressor, this mode presents the similar pattern but possesses smaller amplitude and moves downstream along the impeller streamwise. Figure 15(c) is the structure of 0.067BPF mode in the optimized compressor, this mode is primarily located in the main blade LE, displaying resemblance to the structure of a shock wave.

To elucidate the physical interpretations of the LDF modes for the three compressors, the interplays between mode structures and flow structures are analyzed. Figure 16 shows the spatial patterns of mode structures and flow structures near the impeller inducer. These flow structures correspond to the moment of the 400th flow field sample in DMD analyses. In the figure, the contour represents the mode structures at 95% span, the thick black solid line is the isoline of sound speed (Mach number equals one), the thin red streamlines denote the DLF, and the thin green streamlines represent the TLF. Fig. 16(a) shows that the LFD mode of the solid casing compressor (0.022BPF) is located at the interplay position of the TLF, the DLF and the LE shock wave. Hence, the LFD mode of the solid casing compressor is generated by the strong interplay among the TLF, the DLF and the LE shock wave.

Figure 16(b) illustrates that the LFD mode in the original compressor (0.156BPF) becomes smaller and moves downstream along the streamwise direction. Combining the analyses results of Figs. 10, 11, the reason for the weakness and downstream movement of the LFD mode is due to the suction effect of the P-S. The explanation is as follows. By comparing the three-dimensional streamlines in Fig. 16(a) and (b), it can be found that due to the suction effect of the P-S, some TLF and DLF are removed, and the remaining TLF and DLF in the impeller passage become more uniform. Significant interplay between TLF and DLF occurs only when they move to more downstream regions (away from the LE shock wave). That is to say, the intensity of the interplay between TLF and DLF are decreased, and the location of the strongest interplay region moves downstream. As suggested in Figs. 14 and 15, the energy proportion of the LFD mode in the original compressor decreases and moves downstream. Therefore, the LFD mode of the original compressor is mainly generated by the interplay between the TLF and DLF.

Figure 16(c) shows that the LFD mode pattern in the optimized compressor (0.067BPF) aligns with the LE shock wave. This suggests that the low-frequency dynamic characteristics of the compressor are dominated by the fluctuation of the LE shock wave, instead of the interplay between the TLF and DLF. The mechanism is explainable. As suggested in Figs. 10 and 11, the suction intensity of the P-S of the optimized compressor is further improved, and more TLF and DLF are removed. As a result, throughout the impeller passage, the interplay between TLF and DLF diminishes, while the fluctuation of the LE shock wave emerges as the strongest disturbance. Considering the spatial structure and location of the LFD mode, it can be confirmed that the LFD mode is introduced by the fluctuation of the LE shock wave.

Therefore, the unsteady mechanisms of the flow stability improvement can be summarized as follows: with the growth of the recirculating flow rate of the P-S, more TLF and DLF in the impeller tip region are cleared up, and the interplay intensity among the TLF, DLF and the LE shock wave is reduced. As a result, low-frequency multi-scale modes are hindered from being produced, and the inherent modes are intensified. However, as the recirculating flow rate improves, the suppress effects on low-frequency multi-scale modes are different, resulting in the changes in the frequency and spatial structure of the LFD mode.
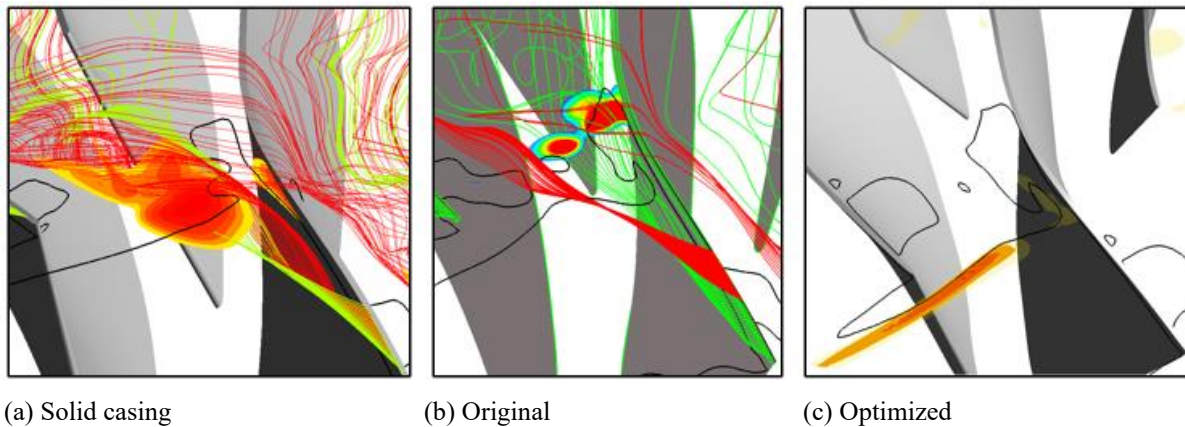
(a) Solid casing   (b) Original   (c) Optimized

Fig. 16 Spatial patterns of the LFD modes and flow structures near impeller inducer under the P₂ working condition

5. CONCLUSIONS AND REMARKS

In this study, a multi-component collaborative optimization of a transonic compressor is conducted, and the unsteady mechanisms of flow stability enhancement are analyzed by the DMD method. The following conclusions can be drawn.

The collaborative optimization method is able to improve the efficiency of the transonic compressor over the entire operating range, the additional aerodynamic losses induced by the P-S can be eliminated. Specifically, compared to the original compressor, the optimized compressor has increased the efficiency by 3.22%, 2.76%, and 1.98% at the PE point (0.881 kg/s), the SFR point (0.840 kg/s), and the NS point (0.792 kg/s) respectively, and has enhanced the stability range by 3.12%. In comparison to the solid casing compressor, the optimized compressor has improved the efficiency by 1.54% and 2.71% at the PE and the SFR points respectively.

The inherent dominant modes of the solid casing, the original and the optimized compressors are BPF and nBPF modes, and they do not affect the flow stability of compressors. The LFD modes of the three compressors are 0.022BPF, 0.156BPF and 0.067BPF respectively, and they are related to the flow instability. The 0.022BPF mode is generated by the strong interplay among the TLF, the DLF and the LE shock wave. The 0.156BPF mode is mainly produced by the interplay between the TLF and DLF. The 0.067BPF mode is introduced by the fluctuation of the LE shock wave. The energy transfer from the inherent modes to the low-frequency modes represents the flow instability process.

The unsteady mechanisms of the flow stability enhancement are: the increased recirculating flow rate of P-S removes more TLF and DLF in impeller tip regions, and then weakens the interplay among the TLF, DLF and the LE shock wave. Consequently, the generation of low-frequency multi-scale modes is suppressed, and the inherent modes are intensified. With the enhancement of the P-S suction effect, the suppression actions on low-frequency multi-scale modes are different, leading to variations in the frequency and spatial structure of the LFD mode.

This study employs single-passage model and URANS numerical method to analyze the flow mechanisms. This is usually limited to the near stall condition. For the fine analyses of unstable flow fields (stall and surge), it usually requires full-passage model and DES (Detached Eddy Simulation) method. This is the authors' future work.

FUNDING

CONFLICT OF INTEREST

The authors declare that they have no known competing financial interests or personal relationships that could have appeared to influence the work reported in this paper.

AUTHORS CONTRIBUTION

T. Zhou：Conceptualization, Data curation, Investigation, Methodology, Software, Visualization, Formal analysis, Writing original draft. **Z. X. Liu:** Supervision, Methodology, Resources. **X. J. Li:** Conceptualization, Methodology, Supervision, Writing review & editing. **M. Zhao:** Validation, Formal Analysis. **Y. J Zhao:** Writing review & editing, Software. **L. C. Xu:** Software.

REFERENCES

Boccazzi, A., Sala, R., & Gaetani, P. (2011). *Influence of the diffuser vane setting angle on the flow field in a radial pump.* Proceedings of the 9th European

Turbomachinery Conference. Istanbul: ETC (pp. 721-731). https://torroja.dmt.upm.es/congresos/etc9_2011/pdf/papers/2011-ETC_9-Paper_133-COLOR.pdf

Cios, K. J., Pedrycz, W., Swiniarski, R. W. (2007). *Data mining and knowledge discovery. Springer Science & Business Media.* https://link.springer.com/chapter/10.1007/978-1-4615-5589-6_1

Ding, S., Chen, S., Wang, S., & Wang, Z. (2022). Flow mechanism of self-recirculating casing treatment in a low-reaction transonic compressor rotor. *Aerospace Science and Technology*, *130*, 107925. https://doi.org/10.1016/j.ast.2022.107925

Favaretto, C. F. F., Anderson, M. R., Li, S., & Hu, L. (2018, June). *Development of a meanline model for preliminary design of recirculating casing treatment in turbocharger compressors*. Turbo Expo: Power for Land, Sea, and Air (Vol. 51173, p. V008T26A006). American Society of Mechanical Engineers. https://doi.org/10.1115/GT2018-75717

Hazy, R. H., & Xu, L. (2009). *Numerical investigation of the effects of leading Edge sweep in a small transonic impeller.* 8th European Turbomachinery Conference. https://scholar.google.com/scholar

He, X., & Zheng, X. (2017). Mechanisms of sweep on the performance of transonic centrifugal compressor impellers. *Applied Sciences*, *7*(10), 1081. https://doi.org/10.3390/app7101081

Huang, G., Yang, Y., Hong, S., Liu, Z., & Du, S. (2020). A new unsteady casing treatment for micro centrifugal compressors to enlarge stall margin. *Aerospace Science and Technology*, *106*, 106176. https://doi.org/10.1016/j.ast.2020.106176

Khaleghi, H. (2020). A new approach of endwall recirculation in axial compressors. *Aerospace Science and Technology*, *98*, 105704. https://doi.org/10.1016/j.ast.2020.105704

Kou, J., & Zhang, W. (2017). An improved criterion to select dominant modes from dynamic mode decomposition. *European Journal of Mechanics-B/Fluids*, *62*, 109-129. https://doi.org/10.1016/j.euromechflu.2016.11.015

Li, X., Liu, Z., & Lin, Y. (2017). Multipoint and multiobjective optimization of a centrifugal compressor impeller based on genetic algorithm. *Mathematical Problems in Engineering*, *2017*(1), 6263274. https://doi.org/10.1155/2017/6263274

Li, X., Liu, Z., & Zhao, Y. (2022a). Redesign of casing treatment for a transonic centrifugal compressor based on a hybrid global optimization method. *Proceedings of the Institution of Mechanical Engineers, Part C: Journal of Mechanical Engineering Science*, *236*(7), 3398-3417. https://doi.org/10.1177/09544062211039878

Li, X., Liu, Z., Zhao, M., Zhao, Y., & He, Y. (2022b).

Stability improvement without efficiency penalty of a transonic centrifugal compressor by casing treatment and impeller/diffuser coupling optimization. *Aerospace Science and Technology*, *127*, 107685. https://doi.org/10.1016/j.ast.2022.107685

Li, X., Zhao, Y., & Liu, Z. (2019). A novel global optimization algorithm and data-mining methods for turbomachinery design. *Structural and Multidisciplinary Optimization*, *60*, 581-612. https://link.springer.com/article/10.1007/s00158-019-02227-5

Li, X., Zhao, Y., Liu, Z., & Zhao, M. (2021). Dynamic mode decomposition analysis of the flow characteristics in a centrifugal compressor with vaned diffuser. *Proceedings of the Institution of Mechanical Engineers, Part A: Journal of Power and Energy*, *235*(1), 154-168. https://doi.org/10.1177/0957650920913464

Lin, F., & Chen, J. (2018). Oscillatory tip leakage flows and stability enhancement in axial compressors. *International Journal of Rotating Machinery*, *2018*(1), 9076472. https://doi.org/10.1155/2018/9076472

Lu, B., Zhu, M., Teng, J., & Qiang, X. (2021). Design strategy of axial slot casing treatment for a transonic compressor rotor based on parametric analysis. *Aerospace Science and Technology*, *119*, 107142. https://doi.org/10.1016/j.ast.2021.107142

Lyu, Z., Kou, J., & Zhang, W. (2022). An experimental modal testing method for subcritical flow around a cylinder. *Physics of Fluids*, *34*(8). https://doi.org/10.1063/5.0101624

Peng, W., Zou, X., & Qin, S. (2021). Design and experiment of casing treatment for a centrifugal compressor. *International Journal of Turbo & Jet-Engines*, *38*(3), 233-244. https://doi.org/10.1515/tjj-2018-0009

Schmid, P. J. (2010). Dynamic mode decomposition of numerical and experimental data. *Journal of Fluid Mechanics*, *656*, 5-28. https://www.cambridge.org/core/journals/journal-of-fluid-mechanics/article/abs/dynamic-mode-decomposition-of-numerical-and-experimental-data/AA4C763B525515AD4521A6CC5E10DBD4

Sesterhenn, J., & Shahirpour, A. (2019). A characteristic dynamic mode decomposition. *Theoretical and Computational Fluid Dynamics*, *33*, 281-305. https://link.springer.com/article/10.1007/s00162-019-00494-y

Shu, M., Yang, M., Deng, K., Zheng, X., & Martinez-Botas, R. F. (2018). Performance analysis of a centrifugal compressor based on circumferential flow distortion induced by volute. *Journal of Engineering for Gas Turbines and Power*, *140*(12), 122603. https://doi.org/10.1115/1.4040681

Taira, K., Brunton, S. L., Dawson, S. T., Rowley, C. W., Colonius, T., McKeon, B. J., Schmidt, O. T., Gordeyev, S., Theofilis, V., & Ukeiley, L. S. (2017). Modal

analysis of fluid flows: An overview. *Aiaa Journal*, *55*(12), 4013-4041. https://doi.org/10.2514/1.J056060

Tamaki, H. (2012). *Effect of recirculation device with counter swirl vane on performance of high pressure ratio centrifugal compressor.* Turbo Expo: Power for Land, Sea, and Air. https://doi.org/10.1115/1.4004820

Tiainen, J., Grönman, A., Jaatinen-Värri, A., & Backman, J. (2017). Flow control methods and their applicability in low-Reynolds-number centrifugal compressors—a review. *International Journal of Turbomachinery, Propulsion and Power*, *3*(1), 2. https://doi.org/10.3390/ijtpp3010002

Trébinjac, I., Kulisa, P., Bulot, N., & Rochuon, N. (2009). *Effect of unsteadiness on the performance of a transonic centrifugal compressor stage*. Turbo Expo: Power for Land, Sea, and Air. 43161, pp.1835-1845. https://doi.org/10.1115/1.3070575

Vo, H. D., Tan, C. S., & Greitzer, E. M. (2008). *Criteria for spike initiated rotating stall.* Turbo Expo: Power for Land, Sea, and Air. 47306, pp.155-165. https://doi.org/10.1115/1.2750674

Wang, W., Chu, W., & Zhang, H. (2018). Mechanism study of performance enhancement in a subsonic axial flow compressor with recirculating casing treatment. *Proceedings of the Institution of Mechanical Engineers, Part G: Journal of Aerospace Engineering*, *232*(4), 680-693. https://doi.org/10.1177/0954410016687140

Wu, Z., Brunton, S. L., & Revzen, S. (2021). Challenges in dynamic mode decomposition. *Journal of the Royal Society Interface*, *18*(185), 20210686. https://doi.org/10.1098/rsif.2021.0686

Xu, L., Liu, Z., Li, X., Zhao, M., & Zhao, Y. (2023a). An improved mode time coefficient for dynamic mode decomposition. *Physics of Fluids*, *35*(10). https://doi.org/10.1063/5.0166272

Xu, L., Liu, Z., Li, X., Zhao, M., Zhao, Y., & Zhou, T. (2023b). Dynamic mode characteristics of flow instabilities in a centrifugal compressor impeller. *Aerospace Science and Technology*, *142*, 108707. https://doi.org/10.1016/j.ast.2023.108707

Yamada, K., Kikuta, H., Furukawa, M., Gunjishima, M., & Hara, Y. (2013). *Effects of tip clearance on the stall inception process in an axial compressor rotor*. Turbo Expo: Power for Land, Sea, and Air. American Society of Mechanical Engineers, 55249: V06CT42A035. https://doi.org/10.1115/GT2013-95479

Yamada, K., Kikuta, H., Iwakiri, K. I., Furukawa, M., Gunjishima, S. (2012). *An explanation for flow features of spike-type stall inception in an axial compressor rotor*. Turbo Expo: Power for Land, Sea, and Air. American Society of Mechanical Engineers, 44748, pp.2663-2675. https://doi.org/10.1115/1.4007570

Yan, S., & Chu, W. (2021). The improvement of transonic compressor performance by the self-circulating casing treatment. *Proceedings of the Institution of Mechanical Engineers, Part C: Journal of Mechanical Engineering Science*, *235*(7), 1165-1176. https://doi.org/10.1177/0954406220942261

Yang, H., Nuernberger, D., Nicke, E., & Weber, A. (2003, January). *Numerical investigation of casing treatment mechanisms with a conservative mixed-cell approach.* Turbo Expo: Power for Land, Sea, and Air (Vol. 36894, pp. 961-974). https://asmedigitalcollection.asme.org/GT/proceedings-abstract/GT2003/961/299470

Zamiri, A., Lee, B. J., & Chung, J. T. (2017). Numerical evaluation of transient flow characteristics in a transonic centrifugal compressor with vaned diffuser. *Aerospace Science and Technology*, *70*, 244-256. https://doi.org/10.1016/j.ast.2017.08.003

Zhang, X., Lu, X., Han, G., Xu, G., & Zhu, J. (2014). Design and Experimental Validation of a High-Pressure Ratio Centrifugal Compressor. *Gas Turbine Technology*, *27*(4), 31-36. https://www.researchgate.net

Zhao, Y., Liu, Z., Fu, L., Zhao, M., & Li, X. (2023). Redesign of a turbocharger compressor based on multi-component full-passage optimization. *Aerospace Science and Technology*, *142*, 108644. https://doi.org/10.1016/j.ast.2023.108644

Zhou, T., Liu, Z., Li, X., Zhao, M., & Zhao, Y. (2021). Thermodynamic design space data-mining and multi-objective optimization of SCO2 Brayton cycles. *Energy Conversion and Management*, *249*, 114844. https://doi.org/10.1016/j.enconman.2021.114844